# Forces driving epithelial wound healing

Agustí Brugués[1*], Ester Anon[1,2*], Vito Conte[1], Jim H. Veldhuis[3], Julien Colombelli[4], José J. Muñoz[5], G. Wayne Brodland[3], Benoit Ladoux[2,6#], Xavier Trepat[1,7,8#]

[1]Institute for Bioengineering of Catalonia, Barcelona, Spain.
[2]Institut Jacques Monod (IJM), Université Paris Diderot, and Unité Mixte de Recherche 7592 CNRS, Paris, France
[3]Department of Civil and Environmental Engineering, University of Waterloo, Waterloo, Ontario, Canada.
[4]Institute for Research in Biomedicine (IRB Barcelona), Barcelona, Spain
[5]Laboratori de Càlcul Numèric, Department of Applied Mathematics III, Universitat Politècnica de Catalunya, Barcelona, Spain.
[6]Mechanobiology Institute (MBI), National University of Singapore, Singapore.
[7]Institució Catalana de Recerca i Estudis Avançats (ICREA), Barcelona, Spain.
[8]Unitat de Biofísica i Bioenginyeria, Facultat de Medicina, Universitat de Barcelona, and CIBERES, Spain

[*] These authors contributed equally to this work

[#] Corresponding authors:

Prof. Xavier Trepat,
Institute for Bioengineering of Catalonia
C/ Baldiri Reixac 15-21
Barcelona 08028
Spain.
Tel: +34934020265
Email: xtrepat@ub.edu

Prof. Benoit Ladoux
Laboratoire Matière et Systèmes Complexes (MSC),
Université Paris Diderot,
7057 Paris, France
Email: benoit.ladoux@univ-paris-diderot.fr

A fundamental feature of multicellular organisms is their ability to self-repair wounds. Central to wound healing is the restoration of a continuous epithelium through the movement of epithelial cells into the damaged area[1,2]. This collective cellular movement is commonly attributed to a combination of cell crawling and "purse-string" contraction of a supracellular actomyosin ring[3-6]. Here we show by direct experimental measurement that these two mechanisms are insufficient to explain force patterns observed during wound closure. Contrary to common assumptions, we found that actin and myosin accumulate at the leading edge in a heterogeneous mechanical structure that transmits part of its tension to the underlying substrate through focal adhesions. The orientation of these adhesions and the traction forces they transmit are mainly parallel to the wound edge and thus perpendicular to the direction of cell motion. This structural and mechanical organization provides cells with an unanticipated mechanism to close the wound by cooperatively compressing the underlying substrate. Our findings establish a quantitative spatiotemporal picture in which subcellular and supracellular cytoskeletal structures cooperate at a multiscale level to drive wound healing.

Wound healing is a central physiological process that involves a complex interplay between inflammation and tissue remodeling[1,2,7]. Impaired wound healing has a significant clinical impact in a variety of widespread diseases such as diabetes, chronic inflammatory disorders, vascular diseases, and auto-immune diseases[1,2,8]. Moreover, there is a well-established association between aberrant wound healing and cancer progression[9].

A crucial step of the wound healing response is the restoration of a continuous epithelial layer to recover tissue homeostasis, regain barrier integrity, and protect organisms from infection[8]. Epithelial repair is achieved through the collective movement of wound-bordering cells into the wound bed. To account for this collective movement, two main mechanisms are commonly invoked[1-3]. The first one is the assembly of a supracellular actomyosin ring at the wound margin, whose contraction drives the wound edges together like a purse-string[5,10-12]. The second mechanism is collective migration of marginal and submarginal cells led by lamellipodial and filopodial protrusions[13-17].

Extensive evidence supports the coexistence of a supracellular actomyosin ring and lamellipodial protrusions at the wound margin[3-6,18]. How these cytoskeletal structures drive wound closure remains incompletely understood, however, because underlying physical forces have not been accessible to direct experimental observation. To provide the first maps of these physical forces, here we combined traction force microscopy and laser ablation. We seeded a monolayer of MDCK cells stably expressing LifeAct-GFP on top of a soft collagen-coated polyacrylamide gel containing fluorescent bead markers. Once the monolayer reached confluence and relatively high density, a cluster of ~20 cells (5000 $\mu m^2$) was ablated by recurrently targeting apical cell surfaces with a sub-nanosecond pulsed laser (Fig. 1a-c, Methods). Immediately after ablation, targeted cells lost a substantial amount of their F-actin content and surrounding cells retracted outwardly.

Following rapid tissue retraction, cells began to invade the wound area and to extrude ablated cells (Supplementary movie 1). The onset of this wound closure phase involved rapid protrusion of lamellipodia and filopodia toward the wound area (Fig. 1d). With a delay of ~15 minutes, cell protrusion was followed by accumulation of actin and myosin at the wound edge (Fig. 1e, g-l). Formation of this supracellular actomyosin ring did not inhibit cell protrusions, which remained visible throughout closure (Fig. 1d-f). Both marginal and submarginal cells progressively acquired an elongated shape and constricted their front edge so as to create a rosette-like geometry by the end of wound closure (Fig. 1f). Throughout the process, cells remained tightly connected to their neighbors through adherens junctions and tight junctions (Supplementary Fig. S1).

To map cell velocities during wound healing we used particle imaging velocimetry on consecutive image pairs. Resulting maps revealed that throughout the closure process cell velocities pointed uniformly towards the wound and were highest at the leading edge (Fig. 1m-p). To analyze systematically the spatiotemporal evolution of cell velocity maps we computed the average radial velocity as a function of distance from the wound edge

and represented this average as spatiotemporal kymographs (Fig. 1q, Supplementary methods). Kymographs confirmed systematic gradients of radial velocity decaying away from the leading edge. However, the velocity of each cell row around the wound exhibited a non-monotonic time evolution (Fig. 1r) with a maximum at ~30 minutes after the onset of wound healing. In contrast with the case of expanding monolayers[19], we did not observe a significant delay in the onset of cell motion between adjacent cell rows, suggesting a mechanism for rapid intercellular coordination specific to wound closure.

To elucidate the mechanisms driving cellular motions we turned to the measurement of cell-substrate traction forces using monolayer traction microscopy[17] (Fig. 2, Supplementary movie 2). The orientation of these forces depended on the curvature of the wound edge. To illustrate this observation we color-coded traction maps based on the sign of their radial component (Fig. 2a-c). Regions of the leading edge exhibiting a convex contour displayed pronounced protrusive activity and traction forces pointing away from the wound (Fig. 2a). By contrast, regions exhibiting a concave contour showed little protrusive activity, an accumulation of actin at the leading edge, and traction forces pointing toward the wound (Fig. 2a). As wound closure progressed, the contour of the leading edge became progressively smoother, and tractions pointing towards the wound became ubiquitous (Fig. 2b,c). The radial component of traction forces increased with wound curvature and, as closure progressed, this dependence became stronger (Fig. 2d).

To isolate systematic force patterns from force fluctuations we computed the average radial ($T_\perp$) and tangential ($T_\parallel$) traction force components as a function of distance from the wound edge. Resulting kymographs displayed a remarkable spatiotemporal force pattern (Fig. 2e,f). At the front of the first cell row, the radial force kymograph exhibited a boundary layer of tractions pointing away from the wound up to the end of the closure process. Immediately behind this boundary layer of outward-pointing tractions, but still within the first cell row, there emerged a second layer with a net inward-pointing component increasing in magnitude with time (Fig. 2e). Tractions within this layer were not purely radial, however, and their tangential component was on average larger than the radial one (Fig. 2f). Further away from the leading edge, traction forces were weak but systematically pointing away from the wound, thus showing that crawling forces are not restricted to the first cell row.

A boundary layer of net outward-pointing tractions, which we refer hereafter as outward-pointing traction layer (OPTL), has been previously observed during the expansion of cellular monolayers[17,20]. It reveals cell crawling led by lamellipodial protrusions[16,17]. By contrast, the observation of a boundary layer of inward pointing traction forces, which we refer hereafter as inward-pointing traction layer (IPTL), is altogether new. These two boundary layers do not originate solely from averaging two distinct cell populations, one comprising cells favoring protrusions and one comprising cells favoring the actomyosin ring. Instead, inward- and outward-pointing tractions were seen to coexist at different distances from the leading edge of individual cells (Fig. 2a-c, g). The coexistence of these two distinct force patterns of opposite sign creates a contractile dipole at the tip of

protruding leading cells. This contractile dipole is absent in single cells migrating in isolation or in cells migrating collectively during monolayer expansion[17,21,22].

A candidate mechanism to explain the IPTL is the transmission of contractile force from the actomyosin ring to the substrate. To study this possibility we first focused on the colocalization of the actomyosin ring and the IPTL. Confocal z-stacks revealed that the actomyosin ring was located basally (Fig. 1g-l, Fig. 2g) and its assembly coincided in time and space with the emergence of the IPTL. This colocalization between the ring and the IPTL persisted throughout the closure process (Fig. 2h). This evidence supports the idea that the IPTL originates from the transmission of contractile forces from the basal ring to the underlying substrate.

To further ascertain the origin of the IPTL, we studied the dynamics of wound closure in the absence of a supracellular actomyosin ring. To prevent ring formation, we treated cells with medium containing 4 mM of calcium chelator EGTA for 1 hour before laser ablation and reduced the concentration to 2 mM during the experiment (Fig. 3, Supplementary movie 3). Calcium chelation weakened cell-cell junctions behind the leading edge but did not fully disrupt them as shown by the presence of E-cadherin and ZO-1 at intercellular contacts (Supplementary Fig. S2). By contrast, calcium chelation prevented the assembly of a supracellular actomyosin ring at the wound edge (Fig 3a-c). Under these conditions, cell velocities at the leading edge were similar in magnitude to control wounds, but submarginal cells moved faster (Fig. 3a-e) and exhibited a loss of directionality (Fig. 3f). Importantly, impairment of the actomyosin ring prevented the emergence of the IPTL (Fig. 3j). Instead, average tractions pointed away from the wound, giving rise to an OPTL that spanned multiple cell rows, which indicates a cell-crawling mechanism involving cooperative force transmission in the radial direction (Fig. 3g-k). Moreover, the dependence of boundary tractions with the edge curvature was lost (Fig. 3l).

Taken together, our findings point to a physical picture in which the OPTL originates from lamellipodial forces, while the IPTL originates from transmission of forces from the ring to the substrate. This physical picture does not explain the striking observation of high tangential tractions at the wound edge, however (Fig. 2b,f). To address this issue we first turned to the structure and localization of focal adhesions. Staining of paxillin revealed two distinct structural patterns. At the leading tip of lamellipodia, paxillin was organized in ellipsoidal clusters whose longest axis was orthogonal to the wound edge (Fig. 4a-d). This organization is characteristic of lamellipodia-driven cell migration[19] and is consistent with the force pattern observed at the OPTL. By contrast, underneath the actomyosin ring paxillin was mainly organized in clusters whose longest axis was parallel to the ring (Fig 4e-h, Supplementary Fig. S3). This structural organization indicates that, contrary to common assumptions, the ring is attached to the substrate through focal adhesions and that these adhesions transmit traction forces in the direction tangential to the wound (Fig. 2b, 2f). To further support this mechanism of force transmission we studied wound closure in LifeAct-Ruby cells expressing talin-GFP (Fig. 4i-k, Supplementary movie 4). These experiments showed that tangential focal adhesions form

at the wound margin and often retain their orientation and localization as the leading edge advances.

Traction forces tangential to the wound would seem counterproductive to drive the cell sheet forward and to extrude damaged cells upwards. Analysis of stresses and displacements within the underlying gel leads to a quite different conclusion, however. By applying a straightforward balance of traction forces as demanded by Newton's laws, we computed the 2D stress tensor ($\sigma$) in the upper surface of the gel substrate. This stress tensor indicates whether the gel is in a tensile or compressive state at any given point and direction of the cell-gel interface (Supplementary Methods). To take into account the geometry of the experiments, we focused on the normal components of $\sigma$ in the directions that are perpendicular ($\sigma_{rr}$) and tangential ($\sigma_{tt}$) to the actomyosin ring. The resulting stress maps, which are not to be confused with traction maps, showed strong spatial heterogeneities under the actomyosin ring with a sharp alternation between compressive and tensile stresses (Fig. 4l,m,o,p). These spatial heterogeneities are inconsistent with current understanding of wound closure mechanisms based on cell crawling or purse-string contraction. Instead, they reveal that the actomyosin ring transmits part of its contractile tension to the substrate as a series of force dipoles oriented tangentially to the wound edge. A fundamental and perhaps counter-intuitive consequence of this mechanical organization is that the underlying gel substrate contracts radially and undergoes a net displacement towards the wound (Fig. 4n,q, Supplement 1, Supplementary Fig. S6a). Thus by applying traction forces tangentially to the wound, cells deform the underlying gel radially so as to steer their motion into the wound area (Supplement 1).

To study the potential of the mechanisms described above to recapitulate the observed wound closure dynamics, we developed a 2-D cellular *in silico* model (Supplement 2). To build the model, lamellipodia and gel tractions were added to a finite element-based γ-μ model of cell mechanics[23,24] (Supplementary Figs. S7, S8). Tensions arising from general cortical contraction and actomyosin ring forces were assumed to act along the cell boundaries while the cytoplasm in the cells was assumed to be viscous and incompressible. Lamellipodia were assumed to arise randomly from any cell edge, but particularly from the edges along the wound perimeter, and to attach to the underlying gel. Viscous drag was assumed to act between the cells and the gel. Under such assumptions, the model shows that the wound can close either through the action of cell crawling or through purse-string contraction; but none of these two mechanisms, or any combination of them, can explain the force patterns observed experimentally. By contrast, the model is able to closely capture experimental force patterns and associated dynamics upon further assuming that the ring contracts heterogeneously and transmits forces to the substrate (Supplement 2, Supplementary Fig. S9).

Our experimental and computational findings establish a quantitative picture of the mechanisms that drive wound closure in an epithelial sheet. Collective cell crawling is responsible for the initial steps of wound closure but the latest stages of the process involve the cooperation between cell crawling and contraction of a supracellular actomyosin ring at the leading edge. Our study reveals that this supracellular ring is a

much more versatile structure than previously thought and serves at least two purposes. First it contributes to wound closure through its well-known purse-string mechanism[1-5,10]. Second, it transmits part of its contractile force to the substrate through focal adhesions that are tangential to the wound. These unanticipated tangential contractile forces induce a displacement of the underlying gel toward the wound area and thus tend to steer the monolayer forward. The substrate displacements are small compared with the wound size, but displacements within this order or magnitude have been shown to steer cell migration through mechanotransduction processes that remain poorly understood[25-27]. The leading edge dynamics and force patterns reported here are qualitatively distinct from any previous observation in single or collective cell systems. As such, they constitute a starting point in the search for new mechanotransduction strategies in wound closure as well as in the broader context of morphogenesis.

## METHODS

### Traction microscopy
Tractions were measured by Fourier-transform traction microscopy with finite gel thickness as described in Trepat et al.[17]. An interrogation window of 32×32 pixels and an overlap of 0.75 were used for the analysis of bead displacements.

### PA gel preparation
Polyacrylamide (PA) gels were prepared by activating glass bottom Petri dishes by incubation with Bind Silane dissolved in acetic acid and ethanol (following the proportion 1:1:14) during 10 min. After rinsing with ethanol, dishes were allowed to air dry. Meanwhile, a mixture of 240 μl NHS, 2.5 μl APS, 0.25 μl TEMED, 12 μl 0.2 μm red beads and 126.4 μl of HEPES 10 mM plus the corresponding volumes of 93.75 μl of acrylamide and 25 μl of bisacrylamide[28] was prepared, to obtain gels of 9 KPa in Young's modulus. 12 μl of this mixture were added to a Petri dish, flattened with an 18 mm glass coverslip and allowed to polymerize for 30 to 45 min. Deionized water was then added to peel off the glass coverslip. Collagen I was added at 0.1 mg/ml and incubated at 4ºC overnight.

### Cell culture
Madin Darby canine kidney (MDCK) II cells and stable cell lines expressing LifeAct-GFP or LifeAct-Ruby were cultured with Dulbecco's modified Eagle's medium supplemented with 10% fetal bovine serum, 100 U/ml of penicillin, 100 μg/ml of streptomycin. Selection antibiotic geneticin was added at 0.5 mg/ml for LifeAct stable cell lines. Cells were maintained at $37^0$C in a humidified atmosphere with 5% of $CO_2$.

### Laser ablation and time-lapse imaging
The set-up used is described in Colombelli et al[29]. After wounding, time-lapse imaging of the gel surface and of the overlying cells was performed using an inverted Nikon confocal microscope, equipped with an incubator to maintain the samples at 37ºC and 5% $CO_2$. The average delay between laser ablation and acquisition of the first image of the time-lapse was ~20 min. Image size was 512×512 pixels. The laser beam caused partial photobleaching of the bead markers but the gel remained largely intact.

**Velocity measurements**
Velocity maps were obtained by PIV with continuous window shift with an interrogation window of 64×64 pixels and overlap of 0.75.

**Transfection**
To image talin during wound closure we used CellLight® talin-GFP. Cells were seeded at low density. When cells were completely attached to the substrate we added 10 μl of the product in 2 ml of medium. Cells were used 16h after transfection.

**Immunofluorescence**
Cells were fixed with 4% paraformaldehyde (in PBS) for 15 min at room temperature (in EGTA experiments paraformaldehyde was diluted in a 4mM EGTA solution). Permeabilization was achieved by incubating with 0.25% Triton X100 (in PBS) for 20 min at room temperature. Cells were saturated with 1% BSA (in PBS) and incubated during 30 min. In the case of Paxillin, 10% FBS (in PBS) was used as blocking solution and cells were incubated during 60 min. Primary antibodies were added with corresponding blocking solution at 1:1000 dilution for ZO-1 and E-cadherin and 1:200 for paxillin and phospho-MLC and incubated for 1-2 hours. Secondary antibodies were added at 1:200 dilution (with 1:1000 of Phalloidin if needed) and incubated for 1-2 hours.

**Figure Captions.**

**Figure 1. Cell morphology and kinematics during wound healing.** (a-c) Scheme of the experimental design. (d-f) Time course of wound closure in LifeAct-GFP MDCK cells. Images are maximum projections of confocal z-stacks. Staining of phalloidin and pMyo at the apical (g-k) and basal (h-l) planes. (m-o) Vectorial representation of cell velocities measured by PIV at the same time points as in d-f. (p) Distribution of the angle $\varphi$ between cell velocities and the direction normal to the wound edge. Data are a pool of all time points for one experiment. (q) Kymograph of the radial component of cell velocities (see methods). (r) Time evolution of cell velocities as a function of the distance from the leading edge. Image acquisition started ~20 min after wounding. Each dataset represents the average radial velocity within concentric rings of width 15 μm (blue for cells located between 0-15 μm from the leading edge, green for 15-30 μm, red for 30-45 μm). Missing time points in (r) are due to image refocusing. Data for these time points have been interpolated in (q) to help visualization. All scale bars are 20μm.

**Figure 2. Traction forces during wound healing.** (a-c) Vectorial representation of traction forces in LifeAct-GFP MDCK cells. Color coding is based on the values of the radial component, with positive forces pointing away from the wound. For clarity, values between 100 and -100 Pa were not plotted. Panels labeled as i and ii show a close-up of the regions indicated by arrows in panels a-c. Scale bar is 20 μm. (d) Radial traction $T_\perp$ as a function of the curvature of the wound edge. The analysis was performed for the three time points shown in panels a (blue), b (green), and c (red). (e) Kymograph for radial traction component $T_\perp$. (f) Kymograph for tangential traction component $T_\parallel$. (g) A confocal z-section of LifeAct-GFP along the dashed line shown in Fig. 2a. Radial and tangential traction forces along that dashed line are shown below LifeAct-GFP images. Total length is 68 μm. (h) Mean radial component of traction (dashed curve) and actin intensity (solid curve) as a function of distance from the center of the wound. Data corresponds to 8 min (blue), 24 min (green) and 44 min (red) after starting acquisition.

**Figure 3. Traction forces in the absence of an actomyosin ring.** (a-c) Vectorial plot of velocities measured by PIV. (d) Kymograph of the radial component of velocities. (e) Time evolution of velocities averaged over adjacent rings of width 15 μm (blue for cells located between 0-15 μm from the leading edge, green for 15-30 μm, red for 30-45 μm). (f) Angular distribution of the angle $\varphi$ between cell velocities and the direction normal to the wound edge. (g-i) Vectorial representation of measured tractions. Color coding is based on the values of the radial component. For clarity, values between 100 and -100 Pa were not been plotted. Kymographs of radial (j) and tangential (k) components of traction forces. (l) Traction as a function of the curvature at the wound edge. The analysis was performed for three time points corresponding to panels g (blue), h (green) and i (red) respectively. All scale bars are 40 μm.

**Figure 4. Force transmission from the ring to the substrate creates heterogeneous stresses and inward-pointing displacements of the underlying substrate.** Representative immunofluorescence micrographs of paxillin and F-actin showing the characteristic structural organization of the leading edge during early (a-d) and late (e-h)

stages of wound closure. During initial stages, focal adhesions were localized at the tip of lamellipodia and were perpendicular to the leading edge (a-d). During later stages, focal adhesions parallel to the leading edge appeared under the actomyosin ring (e-h). Scale bars are 40 μm for a) and e) and 10 μm for b-d and f-k. Time-lapse snap-shots of MDCK cells expressing LifeAct-Ruby and talin-GFP at three different time points of wound closure (see Supplementary movie S4). (l,o) Radial normal stress and (m,p) tangential normal stress in the upper surface of gel during the latest stages of wound closure. (n,q) Radial displacement of the gel surface. Negative displacements point toward the gel. The two time points considered in panels l to q correspond to panels b and c in Fig. 2.

## ACKNOWLEDGEMENTS

## AUTHOR CONTRIBUTIONS

A.B., E.A., J.C., B.L and X.T. designed experiments; A.B. and E.A. performed experiments; A.B., E.A. and V.C. analyzed data; A.B., V.C. and J.J.M. developed computational tools for data and stress analysis; J.C. contributed technology; V.C., J.H.V. and G.W.B built computational models and performed simulations; A.B., E.A., V.C., J.J.M, G.W.B. and X.T wrote the manuscript; all authors discussed and interpreted results and commented on the manuscript; B.L. and X.T. conceived and supervised the project.

## REFERENCES

1    Cordeiro, J. o. V. & Jacinto, A. n. The role of transcription-independent damage signals in the initiation of epithelial wound healing. *Nature Reviews Molecular Cell Biology* **14**, 249-262 (2013).

2    Sonnemann, K. J. & Bement, W. M. Wound Repair: Toward Understanding and Integration of Single-Cell and Multicellular Wound Responses. *Annual Review of Cell and Developmental Biology* **27**, 237-263 (2011).

3    Anon, E. *et al.* Cell crawling mediates collective cell migration to close undamaged epithelial gaps. *Proceedings of the National Academy of Sciences of the United States of America* **109**, 10891-10896 (2012).

4    Klarlund, J. K. Dual modes of motility at the leading edge of migrating epithelial cell sheets. *Proceedings of the National Academy of Sciences* **109**, 15799-15804 (2012).

5    Tamada, M., Perez, T. D., Nelson, W. J. & Sheetz, M. P. Two distinct modes of myosin assembly and dynamics during epithelial wound closure. *The Journal of Cell Biology* **176**, 27-33 (2007).

6    Abreu-Blanco, M. T., Verboon, J. M., Liu, R., Watts, J. J. & Parkhurst, S. M. Drosophila embryos close epithelial wounds using a combination of cellular protrusions and an actomyosin purse string. *Journal of Cell Science* **125**, 5984-5997 (2012).

7    Shaw, T. J. & Martin, P. Wound repair at a glance. *Journal of Cell Science* **122**, 3209-3213 (2009).

8    Crosby, L. M. & Waters, C. M. Epithelial repair mechanisms in the lung. *American Journal of Physiology - Lung Cellular and Molecular Physiology* **298**, L715-L731 (2010).

9    Arwert, E. N., Hoste, E. & Watt, F. M. Epithelial stem cells, wound healing and cancer. *Nature Reviews Cancer* **12**, 170-180 (2012).

10   Hutson, M. S. *et al.* Forces for Morphogenesis Investigated with Laser Microsurgery and Quantitative Modeling. *Science* **300**, 145-149 (2003).

11   Jacinto, A., Woolner, S. & Martin, P. Dynamic Analysis of Dorsal Closure in Drosophila: From Genetics to Cell Biology. *Developmental Cell* **3**, 9-19 (2002).

12   Martin, P. & Lewis, J. Actin cables and epidermal movement in embryonic wound healing. *Nature* **360**, 179-183 (1992).

13   Fenteany, G., Janmey, P. A. & Stossel, T. P. Signaling pathways and cell mechanics involved in wound closure by epithelial cell sheets. *Current Biology* **10**, 831-838 (2000).

14   Omelchenko, T., Vasiliev, J. M., Gelfand, I. M., Feder, H. H. & Bonder, E. M. Rho-dependent formation of epithelial â€œleaderâ€ cells during wound healing. *Proceedings of the National Academy of Sciences* **100**, 10788-10793 (2003).

15   Poujade, M. *et al.* Collective migration of an epithelial monolayer in response to a model wound. *Proceedings of the National Academy of Sciences* **104**, 15988-15993 (2007).

16   Roure, O. d. *et al.* Force mapping in epithelial cell migration. *Proceedings of the National Academy of Sciences of the United States of America* **102**, 2390-2395 (2005).

17   Trepat, X. *et al.* Physical forces during collective cell migration. *Nature Physics* **5**, 426-430 (2009).

18   Meghana, C. *et al.* Integrin adhesion drives the emergent polarization of active cytoskeletal stresses to pattern cell delamination. *Proceedings of the National Academy of Sciences* **108**, 9107-9112 (2011).

19   Serra-Picamal, X. *et al.* Mechanical waves during tissue expansion. *Nature Physics* **8**, 628-634 (2012).

20   Trepat, X. & Fredberg, J. J. Plithotaxis and emergent dynamics in collective cellular migration. *Trends in Cell Biology* **21**, 638-646 (2011).

21   Saez, A. *et al.* Traction forces exerted by epithelial cell sheets. *Journal of Physics: Condensed Matter* **22** (2010).

22   Vedula, S. R. K. *et al.* Emerging modes of collective cell migration induced by geometrical constraints. *Proceedings of the National Academy of Sciences* (2012).

23    Brodland, G. W., Viens, D. & Veldhuis, J. H. A new cell-based FE model for the mechanics of embryonic epithelia. *Computer Methods in Biomechanics and Biomedical Engineering* **10**, 121-128 (2007).

24    H H Chen, G. W. B. Cell-level finite element studies of viscous cells in planar aggregates. *Journal of biomechanical engineering* **122**, 394-401 (2000).

25    Plotnikov, Sergey V., Pasapera, Ana M., Sabass, B. & Waterman, Clare M. Force Fluctuations within Focal Adhesions Mediate ECM-Rigidity Sensing to Guide Directed Cell Migration. *Cell* **151**, 1513-1527 (2012).

26    Reinhart-King, C. A., Dembo, M. & Hammer, D. A. Cell-Cell Mechanical Communication through Compliant Substrates. *Biophysical Journal* **95**, 6044-6051 (2008).

27    Angelini, T. E., Hannezo, E., Trepat, X., Fredberg, J. J. & Weitz, D. A. Cell Migration Driven by Cooperative Substrate Deformation Patterns. *Physical Review Letters* **104** (2010).

28    Yeung, T. *et al.* Effects of substrate stiffness on cell morphology, cytoskeletal structure, and adhesion. *Cell Motility and the Cytoskeleton* **60**, 24-34 (2005).

29    Colombelli, J., Grill, S. W. & Stelzer, E. H. K. Ultraviolet diffraction limited nanosurgery of live biological tissues. *Review of Scientific Instruments* **75**, 472-478 (2004).
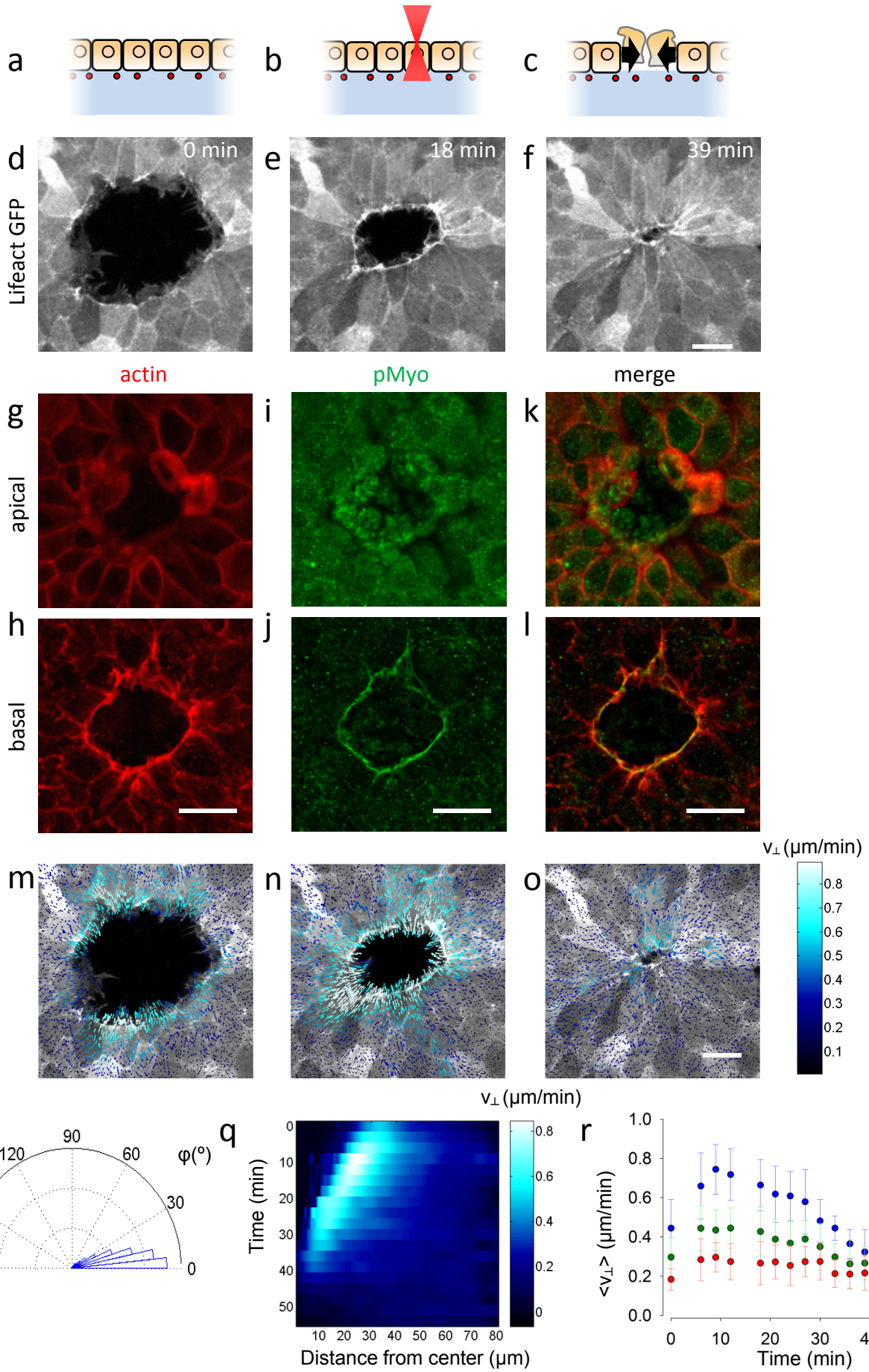
# Figure 1



actin
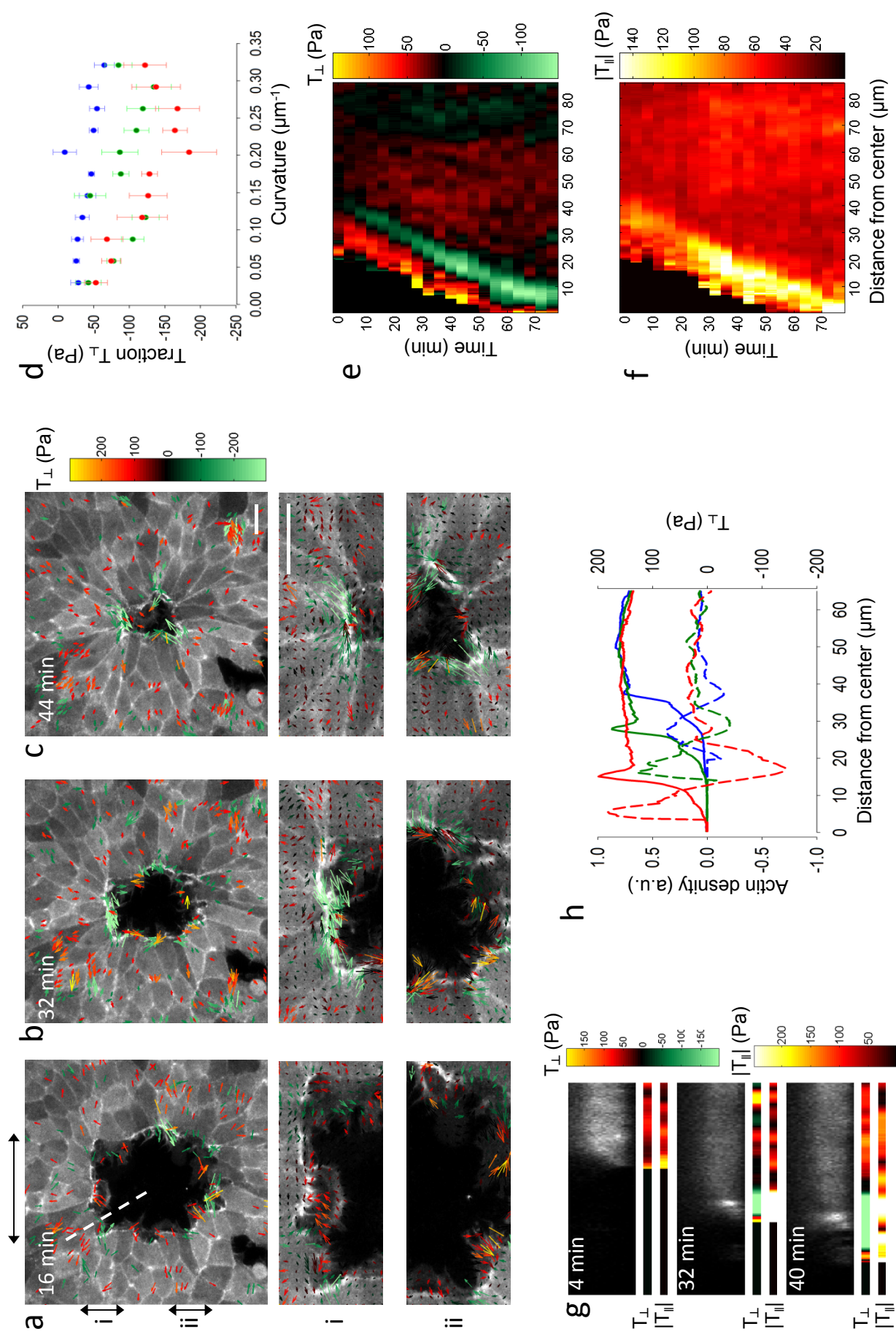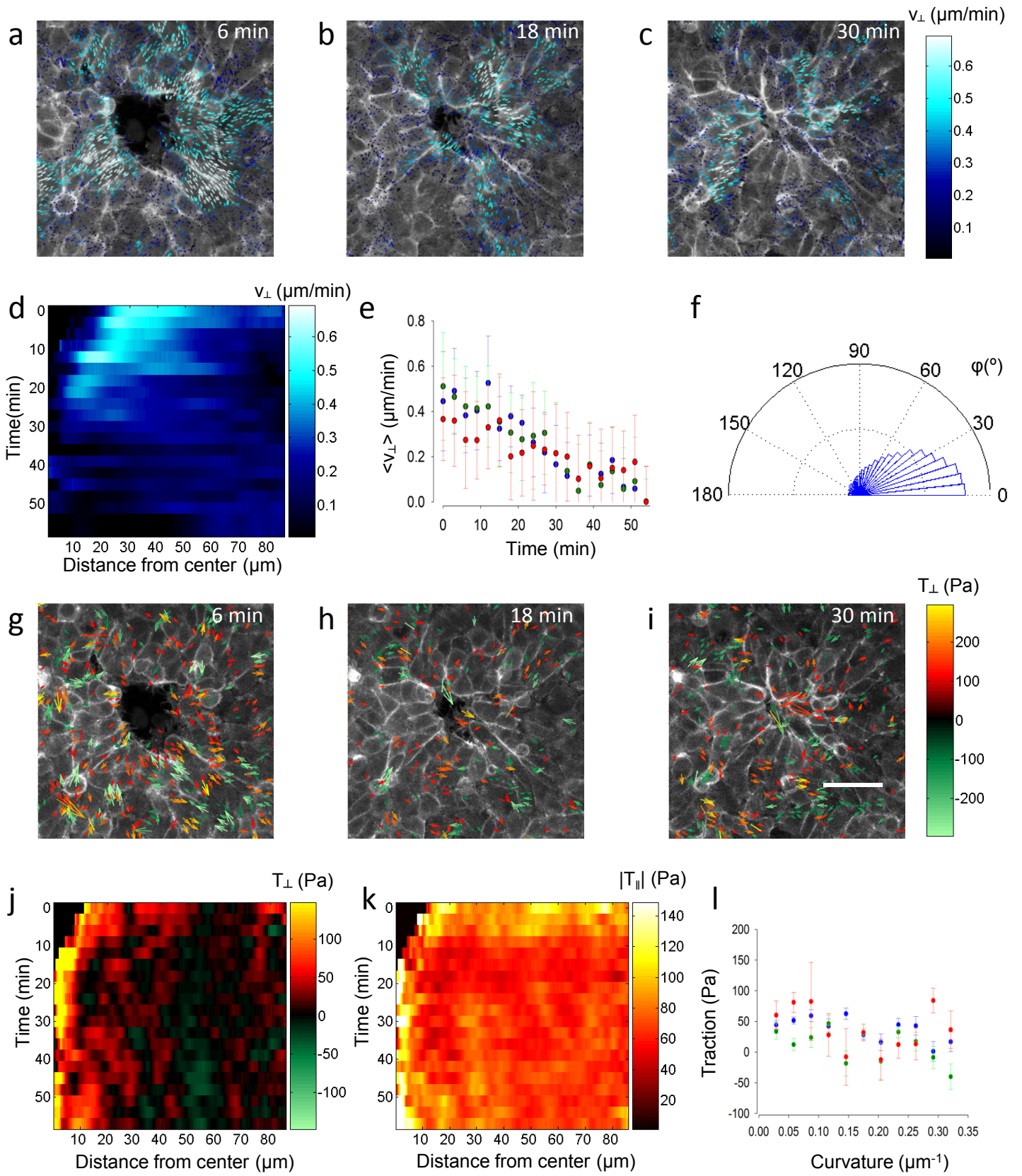
pMyo

merge

apical

basal

$v_\perp$ (µm/min)

$v_\perp$ (µm/min)

$\varphi(°)$

Distance from center (µm)

Time (min)

$\langle v_\perp \rangle$ (µm/min)

Time (min)

Figure 2

# Figure 3

# Figure 4

merge     actin     paxillin     merge

lifeact talin

$\sigma_{rr}$     $\sigma_{tt}$

Pa
200
100
0
-100
-200

μm
0.3
0.2
0.1
0
-0.1
-0.2
-0.3

t = 32 min

t = 44 min